Energy Advances

ROYAL SOCIETY OF CHEMISTRY

PAPER

View Article Online
View Journal

Cite this: DOI: 10.1039/d5ya00133a

Boosting hydrogen production with raspberry-derived carbon aerogels with *in situ* grown carbon nanotubes

Analuisa Rubalcaba-Medina,[a] Fernando J. Rodríguez-Macias,[a] Yunuhem Ameyalli Sanchez-Mendoza,[ab] Sebastián Jiménez-Salinas,[ab] Mouna Rafei,[b] Eduardo Gracia-Espino *[b] and Yadira I. Vega-Cantu *[a]

Received 16th May 2025,
Accepted 20th January 2026

DOI: 10.1039/d5ya00133a

rsc.li/energy-advances

This study explores the use of biomass-based carbon aerogels from raspberry pulp as electrocatalysts for the hydrogen evolution reaction (HER). Producing hydrogen *via* alkaline water electrolysis, from renewable energy sources, is an attractive way to mitigate climate change; however, there still exists challenges in achieving high efficiency without resorting to expensive noble metal catalysts. HER electrocatalysts from transition metal-doped biomass are promising, cost efficient, durable and renewable alternative materials. Freeze dried raspberry pulp with added iron salts was pyrolyzed, resulting in carbon aerogels containing iron oxide nanoparticles. These nanoparticles were later used to grow carbon nanotubes (CNTs) by chemical vapor deposition which enhanced HER activity with overpotential reaching only 408 mV at a current density of −10 mA cm^{-2}, an increase in performance by 30% when compared to that of aerogels without CNTs. This shows that our synthetic approach is effective for catalysis applications, and its versatility means that efficiency could be improved further by tuning the properties of iron oxide nanoparticles and the three-dimensional interconnected porous network of the carbon aerogel.

Introduction

In recent years, there has been a notable surge in interest towards green hydrogen production aimed at facilitating the large-scale implementation of renewable energy-based power plants. Green hydrogen, generated *via* water electrolysis and renewable electricity, offers a carbon-neutral solution to produce hydrogen gas (H_2), which can then be used as a fuel with zero carbon emissions. Consequently, the global demand for green hydrogen and its applications is projected to experience exponential growth over the next decade,[1] with green hydrogen promoted as a way to address climate change issues and overcome the challenges in achieving global net-zero emissions.

Alkaline water electrolysis (AWE) is essential for green hydrogen production, yet it still faces some challenges. AWE is regarded as a well-established technology with a system design favorable for large-scale applications.[2,3] The hydrogen evolution reaction (HER), a crucial half-cell reaction in water splitting, exhibits sluggish kinetics and high overpotentials, requiring the use of electrocatalysts to improve its performance.[4] While Pt-based electrocatalysts currently exhibit superior performance for the HER in acid electrolytes,[5,6] the slow water dissociation reaction required in alkaline water electrolysis makes Ni-based electrocatalysts a good alternative for Pt.[7–10] Efforts are also underway to combine these metals with carbon materials to enhance catalytic performance by combining the excellent electrical conductivity of carbon-based nanomaterials, increasing the number of accessible active sites, and stabilizing metal catalysts against agglomeration and degradation. Additionally, synergistic effects between nanocarbons and metal components can optimize adsorption/desorption properties, while functionalizing nanocarbons with heteroatoms further tunes the electronic structure, all of which contributes to improved catalytic efficiency and durability.[11] Despite the high availability of nanocarbon supports (*e.g.*, carbon black, carbon nanotubes, and graphene) to anchor metal nanoparticles, metal ion leaching or particle aggregation during continuous electrochemical cycling is still a problem.[12] Thus, the development of a highly robust and effective HER electrocatalyst with high tolerance against metal leaching is still desirable.

Carbon aerogels, characterized by their three-dimensional hierarchical porous structures and large specific surface areas,

[a] *Tecnologico de Monterrey, Escuela de Ingeniería y Ciencias, Monterrey, 64849, Mexico. E-mail: yadira.vega@tec.mx*
[b] *Department of Physics, Umeå University, Umeå SE-901 87, Sweden. E-mail: eduardo.gracia@unu.se*

hold significant potential for constructing advanced catalytic materials.[6,13] Traditional carbon aerogels are synthesized *via* the sol–gel polymerization of phenol/resorcinol and formaldehyde, followed by solvent exchange, drying, and high-temperature pyrolysis.[14,15] However, the synthesis of resorcinol relies primarily on benzene, a carcinogenic and volatile material obtained from non-renewable fossil fuels.[16] On the other hand, biomass (*e.g.*, cellulose,[17] chitosan,[18] lignin,[19,20] and biomass waste[21]) has emerged as an important class of precursors for carbon aerogel fabrication, offering abundant, renewable, environmentally friendly, and cost-effective resources.[22] Interestingly, most bio-sourced materials contain elements such as nitrogen and oxygen, resulting in hetero-doped nanostructured carbon materials.[23–25] Freeze-dried fruits form aerogel-like porous structures, making them an attractive option as precursors for porous carbon materials. The use of edible biomass as precursors carries the concern of competition between crops for feeding people and for other uses, but in this regard, it should be noted that there is already a large percentage of fruit biomass being rejected as waste before reaching consumers.[26–28]

We chose raspberries for this study because they have been reported to accumulate more iron and manganese than other fruits and also contain magnesium. These three metals have been reported to work as electrocatalysts over carbon supports.[29–31] Raspberries contain, on average, 0.7 mg of Fe per 100 g of fresh fruit and 0.67 mg of Mn, as well as 22 mg of Mg.[32]

Herein, we present a novel method to produce bio-based carbon aerogels derived from freeze-dried raspberry pulp, doped with iron and further modified through the growth of carbon nanotubes (CNTs) *via* chemical vapor deposition (CVD) which gave promising results for the HER.

Experimental

Materials

Raspberries were purchased from a supermarket and ground manually for preparing aerogels from the fruit puree, as described below; α-cellulose powder (Sigma-Aldrich, CAS # 9004-34-6, bulk density 5.6–6.8 $cm^3\ g^{-1}$) and gelatin granules (Coloidales Duche, Mexico) were used as precursors to prepare the biomass-based aerogels. A standard iron solution was purchased from Fisher Scientific (1000 ppm ± 1%, of iron(III) nitrate CAS # 7782-61-8) and employed as a pre-catalyst for the growth of CNTs. Camphor (Sigma-Aldrich 96%) was used as a carbon precursor during chemical vapor deposition (CVD). All chemicals were of analytical grade and used as received.

Production of bio-based carbon aerogels

Biomass and other components (step 1, Fig. 1) were mixed with water (60 mL) by stirring for 20 min at room temperature. The temperature was then increased to 45 °C, and the mixture was stirred for 20 min more. Heating was stopped and the iron solution was added dropwise, while stirring for 20 min (step 2, Fig. 1). The heating and stirring step at 45 °C helped to better disperse the cellulose and gelatin, as well as to achieve some

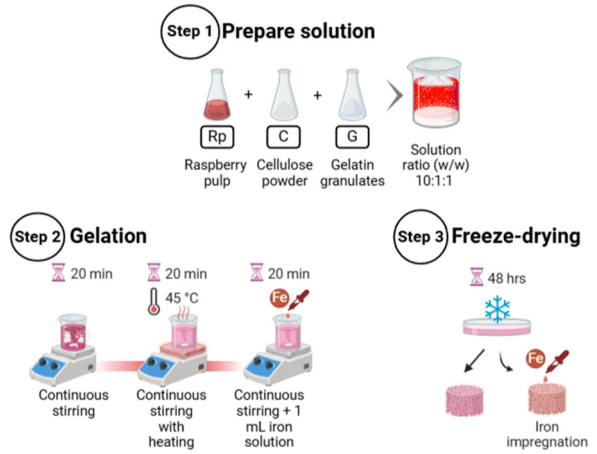

Fig. 1 Schematic illustration of the synthesis process of bio-based carbon aerogels.

gelation of the biomass before freezing. The samples were quickly frozen at −90 °C for 72 h and then freeze-dried (Labconco, FreeZone) for 48 h (step 3, Fig. 1). For some samples, a second addition of Fe was made dropwise over the freeze-dried material, allowing the solution to be absorbed before adding another drop to avoid losing the porous structure. This process continued until full impregnation. These aerogels were then dried under vacuum in a bell jar for a few hours. A variety of bio-based carbon aerogels were produced, with one only containing raspberry pulp (RP, 30 g) as the reference material. Others with RP and cellulose (3 g) were labeled as RP + c, and some with cellulose and gelatin (3 g) were denoted RP + cg. In all samples, 1 mL of iron solution (1000 ppm) was added. The same solution was used for the second addition of Fe (step 3, Fig. 1) to some of the freeze-dried samples (*e.g.* RP + cg + Fe2). The sample content is shown in Table 1.

Two thermal treatments were applied to dry biomass aerogels, simple pyrolysis (step 4a, Fig. 2) or pyrolysis followed by chemical vapor deposition (step 4b, Fig. 2). Aerogel samples were placed in a quartz boat at the center of a horizontal tubular furnace (MTI Corporation, OTF-1200X), in a 45 mm diameter quartz tube. The samples were pyrolyzed under a nitrogen flow of 120 mL min^{-1} at a heating rate of 10 °C min^{-1} from room temperature to 900 °C in all cases. For simple

Table 1 Sample designations according to precursors added to the raspberry pulp (RP) and synthesis procedure. Samples with "+Fe2" designation had the iron precursor added in two steps as explained in the methodology

Label	Precursors added to RP	Thermal treatment
RP-pyr	—	Pyrolysis
RP + c + Fe-pyr	Cellulose, Fe	Pyrolysis
RP + cg + Fe-pyr	Cellulose, gelatin, Fe	Pyrolysis
RP + c + Fe-CVD	Cellulose, Fe	CVD
RP + cg + Fe-CVD	Cellulose, gelatin, Fe	CVD
RP + c + Fe2-CVD	Cellulose, Fe (in 2 steps)	CVD
RP + cg + Fe2-CVD	Cellulose, gelatin, Fe (in 2 steps)	CVD

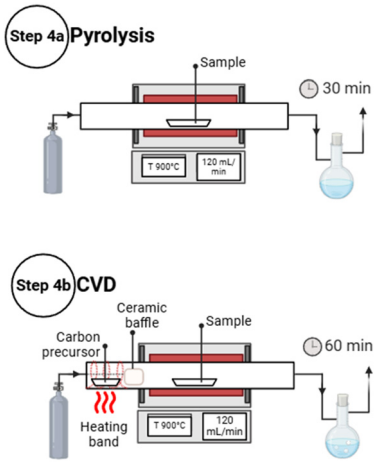

Fig. 2 Schematic illustration of the thermal treatment of bio-based carbon aerogels.

pyrolysis, the samples were then held at 900 °C for 30 min and then allowed to cool down under continuous nitrogen flow. For CVD, camphor was vaporized at *ca.* 120 °C placing 1.1 g about 10 cm away from the entrance of the quartz tube, with a heating band wrapped around the tube. The heating was timed to have the camphor reach the target temperature at the time the tube furnace reached 900 °C. A ceramic cylinder was placed as a baffle to modulate the gas flow at the furnace entrance to prevent premature heating of the camphor and avoid contamination. The sample was kept at 900 °C for 60 min, usually the camphor finished evaporating after ~45 min. The two procedures are illustrated in Fig. 2.

Material characterization

The surface area and porosity of the samples were analyzed by the Brunauer–Emmett–Teller (BET) method with a Quantachrome Autosorb iQ (E-262) N_2 adsorption–desorption instrument. For nitrogen physisorption analysis, all samples were degassed continuously at 80 °C for 2 h, then heated to 200 °C at a rate of 5 °C min^{-1} and maintained at that temperature for 12 h to remove any adsorbed species that could interfere with the adsorption process. X-ray diffraction (XRD) was evaluated with a Bruker Corporation D2 Phaser with CuKα radiation (λ = 0.154 nm). Raman spectroscopy was carried out (Renishaw InVia113P09 CCD Camera) with an excitation wavelength of 633 nm and an exposure time of 10 s. Scanning electron microscopy (SEM, Zeiss EvoMA25) was performed to obtain the morphology of the samples.

Cyclic voltammetry measurements

A standard three-electrode cell was used to evaluate the electrocatalytic properties of the bio-based aerogels using cyclic voltammetry (CV) in a N_2-saturated 1.0 M KOH electrolyte (pH = 14) at room temperature. A glassy carbon electrode with a surface area of 0.192 cm^2 was used to deposit the aerogels as working electrodes. A graphite rod was used as the counter electrode, and Ag/AgCl (3.0 M KCl) as the reference electrode. The data were collected using a potentiostat (Ivium Technologies). The applied voltage was converted to the reversible hydrogen electrode (RHE) using the Nernst equation, where $E_{RHE} = E_{Ag/AgCl} + 0.059 \times pH + E^0_{Ag/AgCl}$. $E_{Ag/AgCl}$ is the potential measured *vs.* Ag/AgCl, $E^0_{Ag/AgCl}$ = 0.210 V for Ag/AgCl. The catalytic activity was measured using CVs at a scan rate of 5 mV s^{-1} in a range of 0.0 to −0.8 V *vs.* RHE. A total of 10 CV cycles were used to achieve a stable polarization curve. The last cathodic scan was used in this work. The stability was evaluated by performing 1000 CV cycles in the range of 0.0 to −0.4 V *vs.* RHE at a scan rate of 100 mV s^{-1}. Electrochemical impedance spectroscopy (EIS) measurements were performed at an overpotential corresponding to a current density of −10 mA cm^{-2} within the frequency range of 10 kHz to 1 Hz with an amplitude of 10 mV. The catalyst ink was prepared by dispersing 5 mg of the bio-carbons in 1.2 mL of a solution containing ethanol and deionized water (1 : 3 volume ratio) and 50 μL of Nafion. The bio-carbon was dispersed by ultrasonication. Afterwards, 20 μL of the aqueous dispersion was drop-cast onto the working electrodes and left to dry under vacuum.

Results and discussion

Characteristics of bio-based aerogels

Seven samples of bio-based aerogels were produced using raspberry pulp, cellulose powder, and gelatin granules, each with a distinct combination of precursors and post-treatment processes, as shown in Table 1 and described in Fig. 1 and 2.

Regarding the second addition of iron, when the solution was added to pure RP, the freeze-dried fruit would hydrate and soften losing its structure, and therefore it was not used for CVD experiments. The aerogels with added gelatin and cellulose did retain the porous structure of the freeze-dried materials while they absorbed the Fe solution, which impregnated the aerogel, and the sample with just cellulose absorbed the solution faster than the ones with cellulose and gelatin.

On average, 64% of the original biomass remained after pyrolysis of pure fruit samples (RP-pyr). For samples containing RP with iron (without cellulose), only 70% of its mass was left after pyrolysis (these samples were not used for electrodes), while 80% was retained in samples containing cellulose (RP + c + Fe-pyr). We can conclude that the presence of cellulose helped with the carbonization, probably because its crystallinity favors graphitization.[33–35] The addition of gelatin (sample RP + cg + Fe-pyr) did not affect significantly the percentage of mass loss. CVD treated samples (RP + c + Fe-CVD and RP + cg + Fe-CVD) had a residual mass of 84%. For those impregnated with iron after freeze-drying (samples with tag ... + Fe2-CVD), the final mass was ~90%. The addition of iron would favor carbonization, but we expect that some of the mass increase after CVD is also due to catalytic carbon deposition, since mass was higher when iron was added in two steps.

The amount of iron coming from the raspberry pulp is expected to be 7 to 10 times that of the fresh fruit (which has, on average, 0.7 of mg Fe per 100 g), considering that the

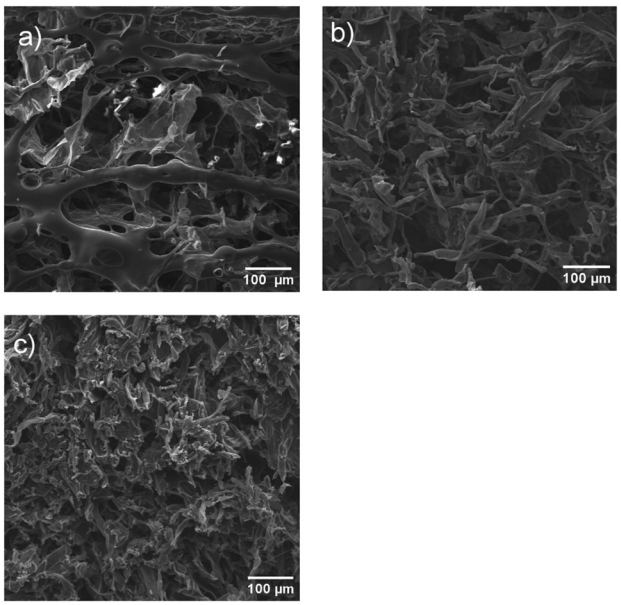

Fig. 3 SEM images of (a) RP-pyr, (b) RP + c + Fe-pyr, and (c) RP + cg + Fe-pyr.

dried mass is 10–15% of the fresh fruit, and about 64% is left after pyrolysis. The measured value by energy dispersive X-ray spectroscopy (EDX) analysis in SEM (further discussed below) was ~0.05 wt% Fe in the pyrolyzed raspberry pulp.

The SEM images of pyrolyzed materials, Fig. 3, display a carbon aerogel structure with 3D hierarchical structures with numerous pores as well as fibrous and sheet-like structures. Some of these features are characteristic of the raspberry biomass precursor as similar features appear in all the other samples. The other bio-based carbon aerogels show fiber-like features which are attributed to the addition of cellulose, with the nanocellulose particles depositing over the pulp pieces.

Similar structures are seen in samples with gelatin, which would suggest that the dissolved gelatin does not segregate and may have formed a thin layer over the RP and cellulose.

Fe nanoparticles were not apparent in pyrolyzed samples, which can be expected since the amount of iron added was relatively small. However, the presence of Fe does result in catalytic growth of carbon nanotubes, as shown in Fig. 4. The second addition of Fe after freeze drying did not result in any significant increase of CNT growth; however, the use of gelatin seems to promote CNT growth. Fig. 5 shows closeups of carbon nanotubes, with most having diameters from 200 to 400 nm, in gelatin-added samples (RP + cg + Fe-CVD and RP + cg + Fe2-CVD). The diameters of the CNTs grown in our system place them at the higher end of the nanoscale range, but they should still contribute to a higher surface area, due to their high aspect ratio, as discussed below.

EDX quantification of iron content (Table 2) reveals that most samples contain <1% Fe, except for the "Fe2" specimens. EDX quantification and elemental mapping results are provided in the SI (Fig. S1). For sample Rp + c + Fe2-CVD, we observed regions that had up to 26% Fe, showing that iron

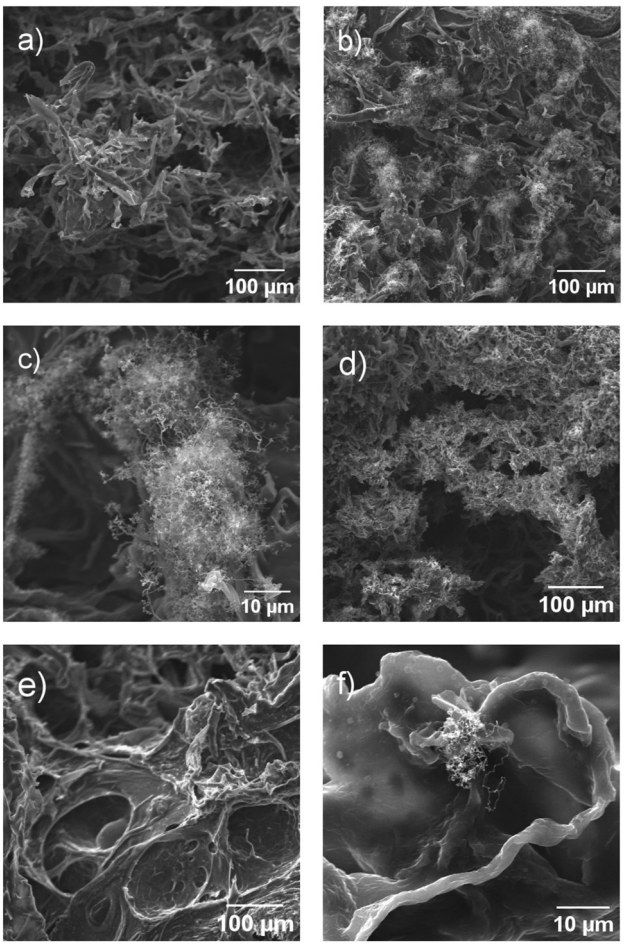

Fig. 4 SEM images of bio-based carbon aerogels: (a) Rp + c + Fe-CVD, (b) and (c) Rp + cg + Fe-CVD, (d) Rp + c + Fe2-CVD, and (e) and (f) Rp + cg + Fe2-CVD.

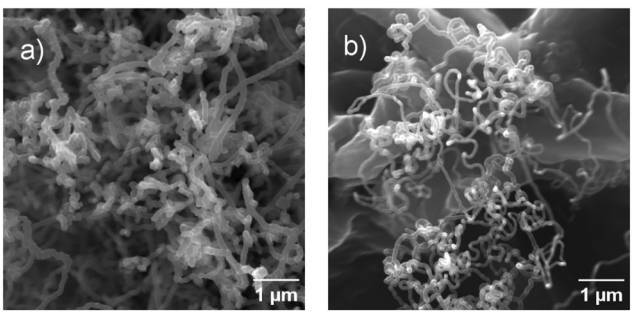

Fig. 5 SEM images of nanotubes observed in bio-based carbon aerogels: (a) RP + cg + Fe-CVD and (b) RP + cg + Fe2-CVD.

segregated to some regions. TGA of a different portion of the same material showed that 6.7 wt% oxides remained after calcination at 900 °C, and iron would be expected to form Fe_2O_3, but some of the residues would be Ca and Mg oxides, which thus would correspond to ≤5 at% Fe. The observation that the Rp + c + Fe2-CVD material absorbed the Fe solution faster than the one with added gelatin can be related to this. We think that the hydrophobic nature of nanocellulose crystals

Table 2 Iron content determined by EDX analysis of pyrolyzed and CVD treated bio-based carbon aerogels

Sample	Fe content (wt%)	CNT growth
RP-pyr	0.05	No
RP + c + Fe-pyr	0.64	No
RP + cg + Fe-pyr	0.04	No
RP + c + Fe-CVD	0.49	No
RP + cg + Fe-CVD	0.43	Yes
RP + c + Fe2-CVD	[a]	Yes (few)
RP + cg + Fe2-CVD	7.46	Yes

[a] Variable, see discussion.

reduces interaction with the iron solution, causing it to pass through the material faster and pooling at the bottom, explaining the heterogeneous composition. As the material dried, the solution would also tend to concentrate away from the nanocellulose crystals, and thus upon thermal treatment, iron atoms coalesced into particles too large to catalyse the growth of CNT, explaining why nanotubes were not seen in samples Rp + c + Fe-CVD and Rp + c + Fe2-CVD (Fig. 4a and d).

We consider that gelatin, being hydrophilic, would help spread better the added iron solution throughout the aerogel, albeit more slowly, leading to a more uniform distribution of iron in the aerogel, and particles with the right size to catalyse nanotube growth. Gelatin could also contribute to spreading iron more uniformly by the interaction of the amino acid functional groups with iron ions. Furthermore, the nitrogen content in gelatin can also help create nitrogen-doped carbon materials during pyrolysis, and nitrogen doping has been reported to be favorable for CNT growth as it creates nucleation sites for metal nanoparticle growth.[36,37] These observations are also consistent with reports of gelatin-derived carbon aerogels exhibiting hierarchical porosity and effective heteroatom incorporation, attributed to the chemical functionalities of gelatin precursors.[38–40] The contrast between the samples with cellulose and those with gelatin indicates that high iron content alone does not ensure CNT growth; rather, dispersion and availability of Fe atoms to form nanoparticles of appropriate size are critical for effective catalytic growth of CNT.

X-ray diffraction and Raman spectroscopy (Fig. 6a) reveal low graphitization of the bio-based carbon aerogels. XRD shows two broad diffraction features centered around 25° and 43.8° which correspond to the (002) and (101) crystal planes of graphitic materials. Diffraction peaks of iron or iron oxides typically appear at 2θ = 30, 35.6, and 38.5°, but these are not apparent in the diffractograms, since the amount of nanoparticles is very small as shown by the EDS analyses. The formation of nanoparticles is inferred from the growth of CNTs, as they would not grow otherwise and are absent in samples without added iron. We did not investigate further the actual composition of the nanoparticles since iron can catalyze the growth of CNTs either as pure metal or in the form of oxides and carbides (cementite), and catalytic Fe nanoparticles usually become oxidized after exposure to air.[41] Knowing the type of material phase in which the iron is present can influence its electrochemical behaviour and may merit further study, but was outside the scope of this work.

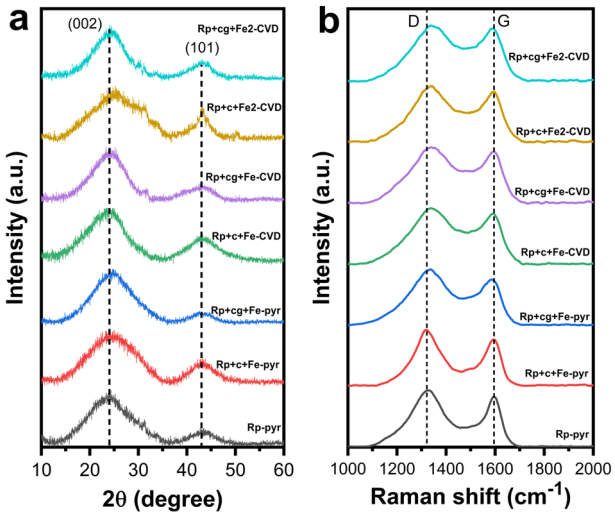

Fig. 6 (a) XRD patterns and (b) Raman spectra of synthesized bio-based carbon aerogels.

Raman spectroscopy (Fig. 6b) shows a broad G band ("graphitic", sp^2 carbon) and a prominent and wide D band ("disorder", sp^3 carbon). This indicates that the biocarbon in these samples is mostly amorphous, which agrees with the low crystallinity shown by XRD. The relative intensities of the D and G, the I_D/I_G ratio can indicate differences in relative graphitization or suggest the presence of more graphitic materials (*e.g.* multi-walled carbon nanotubes), but the values for these samples (Table 3) do not reveal a clear trend: the lowest intensity (I_D/I_G = 1.06) was for RP + cg + Fe-CVD, but it was almost the same as the sample after CVD treatment without iron (1.08, RP + cg + Fe-CVD, I_D/I_G = 1.06), while the equivalent sample subjected to pyrolysis but not to CVD (RP + cg + Fe-pyr) had the highest ratio (I_D/I_G = 1.22).

The specific surface area, pore size, and pore distribution of the aerogels were measured using N_2 adsorption/desorption isotherms (Fig. 7). The results show adsorption/desorption type IV isotherms characterized by the uptake at low p/p_0 (less than 0.1) and the hysteresis above p/p_0 of 0.7, indicating the presence of a mesoporous structure. Compared with pyrolyzed samples, a more pronounced uptake tendency of CVD samples was observed at high relative pressure (p/p_0 = 0.9–1.0), indicative of the presence of interconnected meso- and macropores.[42] The absorbed N_2 volume of the CVD samples decreased, likely due to the increase in pore size during the thermal process.

Table 3 Position and intensity ratios of the D and G bands of Raman spectra

Sample	D band (cm^{-1})	G band (cm^{-1})	I_D/I_G
RP-pyr	1331	1595	1.12
RP + c + Fe-pyr	1318	1594	1.20
RP + cg + Fe-pyr	1333	1585	1.22
RP + c + Fe-CVD	1337	1590	1.11
RP + cg + Fe-CVD	1338	1593	1.08
RP + c + Fe2-CVD	1338	1592	1.12
RP + cg + Fe2-CVD	1338	1589	1.06

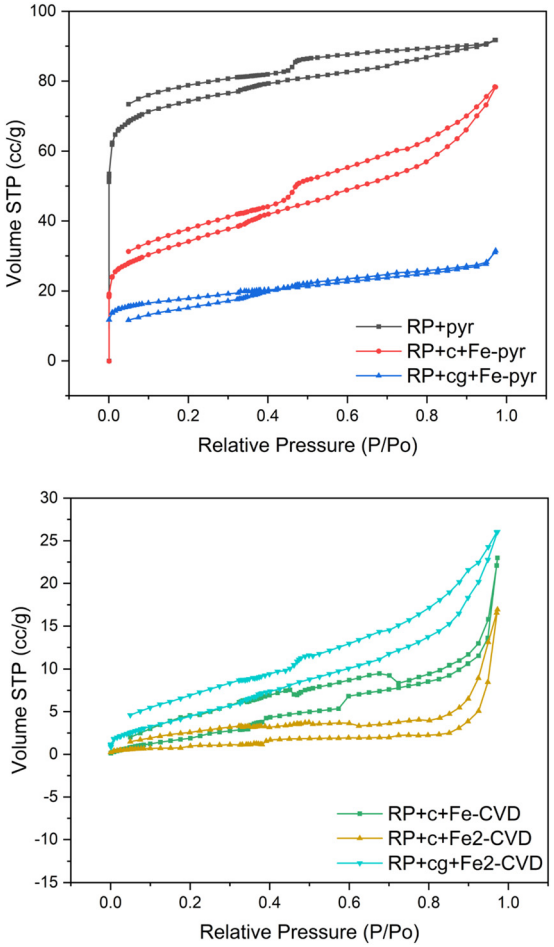

Fig. 7 Nitrogen sorption isotherms for bio-based carbon aerogels subjected to (a) pyrolysis and (b) CVD treatment.

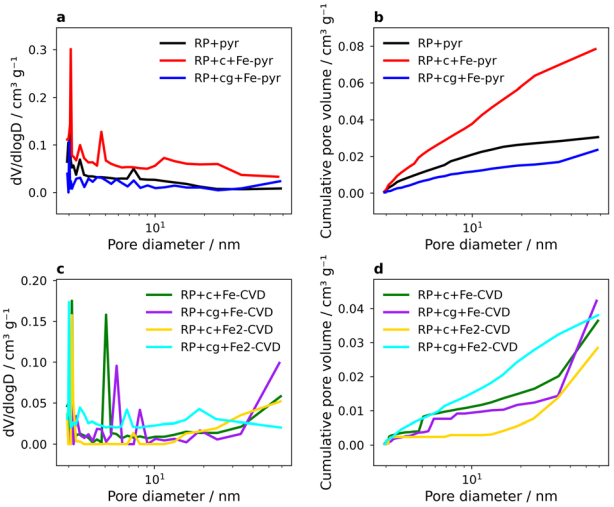

Fig. 8 (a) BJH pore size distribution (PSD) of pyrolyzed aerogels. (b) Cumulative pore volume of pyrolyzed aerogels. (c) BJH PSD of CVD-modified aerogels. (d) Cumulative pore volume of CVD-modified aerogels. PSD curves were obtained from the desorption branch of the N_2 sorption isotherms using the BJH method.

As summarized in Table 4, the carbonized samples (RP-pyr, RP + c + Fe-pyr and RP + cg + Fe-pyr) exhibited higher surface areas attributed to the generation of porosity by the removal of the organic groups during thermal treatment. In contrast, CVD treatment reduced the surface area, suggesting that the deposition of carbon may be closing some pores.

Table 4 Pore measurement of bio-based carbon aerogels derived from N_2 sorption at 77 K. S_{BET} calculated using the BET method; V total from the BJH cumulative pore volume; modal pore size from BJH PSD (desorption branch); median pore size at a 50% cumulative volume; and average pore diameter from 4 V A^{-1}. *The RP + cg + Fe-CVD sample had SBET <1 m^2 g^{-1}

Sample	S_{BET} (m^2 g^{-1})	V total (cm^3 g^{-1})	Modal pore size (nm)	Median pore size (nm)	Average pore diameter (nm, 4 V A^{-1})
RP-pyr	286.65	0.03	3.04	6.76	0.43
RP + c + Fe-pyr	121.61	0.08	3.08	10.42	2.58
RP + cg + Fe-pyr	65.91	0.02	3.02	10.15	1.43
RP + c + Fe-CVD	9.40	0.04	3.14	28.84	15.49
RP + cg + Fe-CVD	<1.00*	0.04	57.94	39.56	—
RP + c + Fe2-CVD	2.81	0.03	3.13	34.39	40.46
RP + cg + Fe2-CVD	20.45	0.04	3.01	14.00	7.44

For the samples with cellulose and without gelatin, the BET surface area is smaller probably because camphor can undergo thermal decomposition into amorphous carbon,[43] while in the samples with added gelatin iron nanoparticles would instead convert most of it into nanotubes, which provide additional surface area.

To gain further insight into the pore structure, the Barrett–Joyner–Halenda (BJH) method was used to calculate pore-size distributions and cumulative pore volumes from the desorption branch of the isotherms (Fig. 8). The corresponding textural parameters are reported in Table 4. Pyrolyzed samples exhibited broad mesopore distributions and higher cumulative pore volumes, consistent with the development of open porosity during carbonization. Conversely, CVD-modified samples displayed lower cumulative pore volumes and a shift of the distribution toward smaller diameters, particularly in the Fe2-CVD aerogels. These findings indicate that carbon deposition by CVD narrowed or blocked mesopores. Taken together, the BET and BJH analyses provide a comprehensive picture of the aerogel architecture resulting from different synthesis routes: pyrolysis promotes accessible mesoporosity and higher surface areas, whereas CVD limits pore accessibility, potentially enhancing confinement and active-site dispersion at the expense of diffusion pathways.

Electrocatalytic activity towards the HER

The catalytic activity of the bio-based carbon aerogels towards the HER was evaluated in a three-electrode cell filled with 1 M N_2-saturated KOH, see details in the experimental section. The polarization curves and Tafel slopes are shown in Fig. 9. The aerogels produced with only raspberry RP-pyr exhibit an overpotential to achieve a current density of -10 mA cm^{-2} (η_{10}) of 588 mV. The value of η_{10} is used as the figure-of-merit to evaluate the electrocatalytic activity since it is a measure of

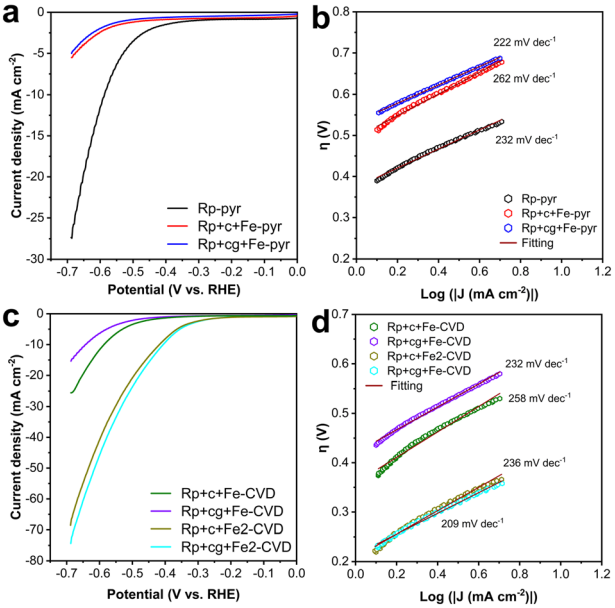

Fig. 9 Electrocatalytic performance towards the hydrogen evolution reaction of bio-based carbon aerogels. (a) Polarization curves and (b) Tafel slope of aerogels subjected to pyrolysis. (c) Polarization curves and (d) Tafel slope of aerogels subjected to CVD.

the current density expected at the electrode using a 10% efficient solar water-splitting device under one sun illumination. The Tafel slope for the RP-pyr aerogel is 232 mV dec^{-1}, as shown in Fig. 9a and b. The value of the Tafel slope is indicative of the reaction pathways. Tafel slopes of 120 mV dec^{-1} or larger indicate that the rate determining step is the Volmer reaction ($H^+ + e^- \rightarrow H_{ads}$), suggesting that these materials have a weak interaction with hydrogen.[44] The HER activity of RP-pyr likely originated from the defects present in the graphitic structure[45] and the natural content of iron. The addition of cellulose (RP + c + Fe-pyr) and gelatin (RP + cg + Fe-pyr) results in a reduction in the HER performance as these samples are not able to reach a current density of -10 mA cm^{-2} in the selected potential range. Samples subjected to the CVD process, Fig. 9c and d, exhibit better HER performance as all aerogels reached -10 mA cm^{-2}. The RP + c + Fe2-CVD and RP + cg + Fe2-CVD aerogel, both containing additional iron, exhibited the lowest η_{10} of 421 mV and 408 mV, respectively, a significant decrease of $\sim$180 mV when compared to RP-pyr. This enhanced HER activity is expected not only because of the increased Fe content and the interaction between iron and the bio-based carbon aerogels[46] but also due to the presence of carbon nanotubes that can enhance the electron transport characteristics. The values of the Tafel slopes remained similar ($>$200 mV dec^{-1}) among different bio-carbons, indicating that the rate-determining step remains unchanged.

EIS studies (Fig. S2) reveal that the RP + cg + Fe2-CVD aerogel exhibits better electron transport characteristics as seen by a lower ohmic resistance of only 1.7 Ω cm^2, compared to 4.1 Ω cm^2 for the Rp-pyr aerogel (see Table S1). Therefore, the HER activity is mainly improved due to an enhanced conductivity and reduced overpotential. The latter is indicative of a larger availability of active sites promoted by the second addition of Fe during the synthesis process. The HER activity of the RP + cg + Fe2-CVD aerogel was maintained even after the stability test (1000 CVs, 0.0–0.4 V *vs.* RHE, 100 mV s^{-1}), with an increase of only 14 mV for the value of η_{10} (Fig. S3). A summary of the HER performance is given in Table S2.

A full understanding of the effect of Fe on the electrocatalytic behaviour may require knowing in which form it is present. However, iron, being in relatively small weight percentages in a porous aerogel, makes such determination challenging. Additionally, iron can also participate in redox reactions changing from Fe° to Fe(II) and Fe(III) during electrochemical measurements.[47] Furthermore, as mentioned above, oxidation on air exposure may result in a different phase during measurements than the one present during the catalysis experiments.

The observed HER performance (η_{10} = 408 mV at -10 mA cm^{-2}) places the RP + cg + Fe2-CVD aerogel within the range of recently reported biomass-derived carbon electrocatalysts. For instance, a CO_2-assisted N-doped carbon aerogel with Ni–Co nanoparticles achieved an overpotential as low as 179 mV under alkaline HER conditions.[48] Meanwhile, biochar aerogels decorated with Ru/RuS_2 have shown overpotentials around 228 mV for OER catalysis.[49] Though direct analogues to our system are scarce, these examples highlight the potential of advanced carbon aerogel designs for high-performance electrocatalysis.[50] Our Fe-based system stands out for combining renewable biomass sourcing with earth-abundant metal catalysis and structural enhancement *via* CNT integration.

Conclusions

This study demonstrates the potential of bio-based carbon aerogels as efficient and sustainable electrocatalysts for the hydrogen evolution reaction in alkaline environments. Using iron-impregnated raspberry pulp as the precursor, we synthesized aerogels with a three-dimensional porous structure decorated with CNTs grown *via* CVD. The inclusion of CNTs significantly enhanced HER activity, as evidenced by a 30% increase in performance compared to aerogels without nanotubes, achieving an overpotential of 408 mV at -10 mA cm^{-2}. The natural iron content of raspberry pulp likely contributed to the intrinsic HER activity of its aerogel, which highlights the catalytic potential of bio-derived materials. While the addition of cellulose did not improve HER performance, the reduced BET surface area of iron-impregnated samples indicates that catalytic activity stems primarily from active iron sites rather than the increased surface area.

A full explanation of how iron contributes to electrocatalytic activity would require further work; nevertheless, this study proves that it is advantageous to add it to biomass based aerogels. When compared with recent biomass-derived, transition-metal-doped carbon aerogels, our Fe-based catalyst demonstrates competitive electrocatalytic performance achieving 408 mV while benefiting from the greater abundance, lower

cost, and reduced toxicity of iron. This positions Fe-based biomass-derived aerogels as sustainable, high-performance alternatives for HER catalysis. The integration of CNTs further enhances electron transport and active site accessibility, contributing to the observed activity boost.

Overall, these results establish a cost-effective and environmentally friendly pathway for fabricating high-performance HER catalysts. The combination of a renewable biomass precursor, abundant iron, and nanocarbon architecture provides a versatile platform for future catalyst design, not only for hydrogen production but also for broader electrocatalytic and renewable energy applications.

Author contributions

ARM: conceptualization, investigation, methodology, formal analysis, visualization, writing – original draft, and writing – review and editing. FJRM: formal analysis, conceptualization, supervision, methodology, resources, and writing – review and editing. YASM and SJS: investigation and methodology. MR: methodology, formal analysis, and visualization. EGE: conceptualization, methodology, supervision, writing – original draft, and writing – review and editing. YIVC: project administration and supervision – review and editing.

Conflicts of interest

There are no conflicts to declare.

Data availability

The data supporting this article have been included as part of the supplementary information (SI), including elemental quantification and composition mapping by EDS and electrochemical data. See DOI: https://doi.org/10.1039/d5ya00133a.

Acknowledgements

This research was supported by Tecnologico de Monterrey and Umeå University. ARM acknowledges PhD scholarship support from SECIHTI (grant 921498). FJRM acknowledges SECIHTI support (grant A1-S-43933). EGE acknowledges support from the Kempe Foundation (JCK-2132), the Carl Trygger Foundation (CTS 21-1581), the Olle Engkvist Foundation (219-0116), and the Swedish Foundation for Strategic Research (SSF-Agenda 2030 – PUSH). We also thank the Vibrational Spectroscopy Core Facility (ViSp) at Umeå University. We are grateful to Regina Elizabeth Vargas-Mejía, Priscila Sepúlveda-Mireles, and Dr. Nancy Edith Ornelas-Soto for their support with characterization at Tecnológico de Monterrey and to Martín Pedro Regules-Aburto and Emiliano Bautista-Barrios from Tecnológico de Monterrey for help in acquiring electrochemical data in a work visit at Umea University.

References

1 S. Shiva Kumar and H. Lim, An overview of water electrolysis technologies for green hydrogen production, *Energy Rep.*, 2022, **8**, 13793–13813.
2 X. Ge, A. Sumboja, D. Wuu, T. An, B. Li, F. W. T. Goh, T. S. A. Hor, Y. Zong and Z. Liu, Oxygen Reduction in Alkaline Media: From Mechanisms to Recent Advances of Catalysts, *ACS Catal.*, 2015, **5**, 4643–4667.
3 O. O. Fashedemi, A. Bello, T. Adebusuyi and S. Bindir, Recent trends in carbon support for improved performance of alkaline fuel cells, *Curr. Opin. Electrochem.*, 2022, **36**, 101132.
4 S. Lai, C. Lv, S. Chen, P. Lu, X. She, L. Wan, H. Wang, J. Sun, D. Yang and X. Zhao, Ultrathin nickel phosphide nanosheet aerogel electrocatalysts derived from Ni-alginate for hydrogen evolution reaction, *J. Alloys Compd.*, 2020, **817**, 152727.
5 T. He, Y. Song, Y. Chen, X. Song, B. Lu, Q. Liu, H. Liu, Y. Zhang, X. Ouyang and S. Chen, Atomically dispersed ruthenium in carbon aerogels as effective catalysts for pH-universal hydrogen evolution reaction, *Chem. Eng. J.*, 2022, **442**, 136337.
6 Z. Al-Hamamre, Z. Karimzadeh, S. Ji, H. Choi and H. Maleki, Aerogels-Inspired based Photo and Electrocatalyst for Water Splitting to Produce Hydrogen, *Appl. Mater. Today*, 2022, **29**, 101670.
7 J. Zhang, T. Wang, P. Liu, Z. Liao, S. Liu, X. Zhuang, M. Chen, E. Zschech and X. Feng, Efficient hydrogen production on $MoNi_4$ electrocatalysts with fast water dissociation kinetics, *Nat. Commun.*, 2017, **8**, 15437.
8 X. Wu, A. Piñeiro-García, M. Rafei, A. Kuzhikandathil, E. J. Canto-Aguilar and E. Gracia-Espino, Highly Active and Durable Nanostructured Nickel-Molybdenum Coatings as Hydrogen Electrocatalysts via Solution Precursor Plasma Spraying, *ChemistryOpen*, 2025, **14**(1), e202400069.
9 X. Wu, A. Piñeiro-García, M. Rafei, N. Boulanger, E. J. Canto-Aguilar and E. Gracia-Espino, Scalable production of foam-like nickel–molybdenum coatings via plasma spraying as bifunctional electrocatalysts for water splitting, *Phys. Chem. Chem. Phys.*, 2023, **25**, 20794–20807.
10 W. Ma, X. Zhang, W. Li, M. Jiao, L. Zhang, R. Ma and Z. Zhou, Advanced Pt-based electrocatalysts for the hydrogen evolution reaction in alkaline medium, *Nanoscale*, 2023, **15**, 11759–11776.
11 Y. Xue, L. Xu, M. Chen, C. Wu, G. Cheng, N. Wang and X. Hu, Constructing Ni-based confinement catalysts with advanced performances toward the CO_2 reforming of CH_4: state-of-the-art review and perspectives, *Catal. Sci. Technol.*, 2021, **11**, 6344–6368.
12 D. K. Sam, W. Wang, S. Gong, E. K. Sam, X. Lv, J. Wang and J. Liu, CO_2 assisted synthesis of silk fibroin driven robust N-doped carbon aerogels coupled with nickel–cobalt particles as highly active electrocatalysts for HER, *Int. J. Hydrogen Energy*, 2021, **46**, 21525–21533.
13 S. Yu, S. Song, R. Li and B. Fang, The lightest solid meets the lightest gas: an overview of carbon aerogels and their

composites for hydrogen related applications, *Nanoscale*, 2020, **12**, 19536–19556.
14 G. Veselov and A. Vedyagin, Resorcinol–Formaldehyde-Derived Carbon Xerogels: Preparation, Functionalization, and Application Aspects, *Materials*, 2023, **16**, 6566.
15 J.-H. Lee and S.-J. Park, Recent advances in preparations and applications of carbon aerogels: A review, *Carbon*, 2020, **163**, 1–18.
16 D. K. Sam, E. K. Sam, A. Durairaj, X. Lv, Z. Zhou and J. Liu, Synthesis of biomass-based carbon aerogels in energy and sustainability, *Carbohydr. Res.*, 2020, **491**, 107986.
17 H. Zhuo, Y. Hu, X. Tong, L. Zhong, X. Peng and R. Sun, Sustainable hierarchical porous carbon aerogel from cellulose for high-performance supercapacitor and CO_2 capture, *Ind. Crops Prod.*, 2016, **87**, 229–235.
18 L. Wang, Q. Wu, B. Zhao, Z. Li, Y. Zhang, L. Huang and S. Yu, Multi-functionalized carbon aerogels derived from chitosan, *J. Colloid Interface Sci.*, 2022, **605**, 790–802.
19 C.-W. Wu, P.-H. Li, Y.-M. Wei, C. Yang and W.-J. Wu, Review on the preparation and application of lignin-based carbon aerogels, *RSC Adv.*, 2022, **12**, 10755–10765.
20 M. A. Karaaslan, L.-T. Lin, F. Ko and S. Renneckar, Carbon Aerogels From Softwood Kraft Lignin for High Performance Supercapacitor Electrodes, *Front. Mater.*, 2022, **9**, 894061.
21 L. Zhu, Y. Wang, Y. Wang, L. You, X. Shen and S. Li, An environmentally friendly carbon aerogels derived from waste pomelo peels for the removal of organic pollutants/oils, *Microporous Mesoporous Mater.*, 2017, **241**, 285–292.
22 J.-H. Lee and S.-J. Park, Recent advances in preparations and applications of carbon aerogels: A review, *Carbon*, 2020, **163**, 1–18.
23 Q. Wu, J. Hu, S. Cao, S. Yu and L. Huang, Heteroatom-doped hierarchical porous carbon aerogels from chitosan for high performance supercapacitors, *Int. J. Biol. Macromol.*, 2020, **155**, 131–141.
24 J. Du, L. Liu, Z. Hu, Y. Yu, Y. Zhang, S. Hou and A. Chen, Raw-Cotton-Derived N-Doped Carbon Fiber Aerogel as an Efficient Electrode for Electrochemical Capacitors, *ACS Sustainable Chem. Eng.*, 2018, **6**, 4008–4015.
25 F. Zhang, T. Liu, J. Zhang, E. Cui, L. Yue, R. Jiang and G. Hou, The potassium hydroxide-urea synergy in improving the capacitive energy-storage performance of agar-derived carbon aerogels, *Carbon*, 2019, **147**, 451–459.
26 Y. K. Leong and J.-S. Chang, Valorization of fruit wastes for circular bioeconomy: Current advances, challenges, and opportunities, *Bioresour. Technol.*, 2022, **359**, 127459.
27 M. Râpă, R. N. Darie-Nita and G. Coman, Valorization of Fruit and Vegetable Waste into Sustainable and Value-Added Materials, *Waste*, 2024, **2**, 258–278.
28 K. S. Ganesh, A. Sridhar and S. Vishali, Utilization of fruit and vegetable waste to produce value-added products: Conventional utilization and emerging opportunities-A review, *Chemosphere*, 2022, **287**, 132221.
29 B. Zhang, J. Zhang, J. Shi, D. Tan, L. Liu, F. Zhang, C. Lu, Z. Su, X. Tan, X. Cheng, B. Han, L. Zheng and J. Zhang, Manganese acting as a high-performance heterogeneous electrocatalyst in carbon dioxide reduction, *Nat. Commun.*, 2019, **10**, 2980.
30 S. Liu, Z. Li, C. Wang, W. Tao, M. Huang, M. Zuo, Y. Yang, K. Yang, L. Zhang, S. Chen, P. Xu and Q. Chen, Turning main-group element magnesium into a highly active electrocatalyst for oxygen reduction reaction, *Nat. Commun.*, 2020, **11**, 938.
31 T. Sun, Q. Wu, O. Zhuo, Y. Jiang, Y. Bu, L. Yang, X. Wang and Z. Hu, Manganese oxide-induced strategy to high-performance iron/nitrogen/carbon electrocatalysts with highly exposed active sites, *Nanoscale*, 2016, **8**, 8480–8485.
32 M. Y. Akimov, V. A. Koltsov, E. V. Zhbanova and O. M. Akimova, Nutritional value of promising raspberry varieties, *IOP Conf. Ser. Earth Environ. Sci.*, 2021, **640**, 022078.
33 C. Chen, K. Sun, A. Wang, S. Wang and J. Jiang, Catalytic graphitization of cellulose using nickel as catalyst, *BioResources*, 2018, **13**, 3165–3176.
34 N. Paksung, J. Pfersich, P. J. Arauzo, D. Jung and A. Kruse, Structural Effects of Cellulose on Hydrolysis and Carbonization Behavior during Hydrothermal Treatment, *ACS Omega*, 2020, **5**, 12210–12223.
35 D.-Y. Kim, Y. Nishiyama, M. Wada and S. Kuga, Graphitization of highly crystalline cellulose, *Carbon*, 2001, **39**, 1051–1056.
36 X. Lepró, E. Terrés, Y. Vega-Cantú, F. J. Rodríguez-Macías, H. Muramatsu, Y. A. Kim, T. Hayahsi, M. Endo, M. Torres and M. Terrones, Efficient anchorage of Pt clusters on N-doped carbon nanotubes and their catalytic activity, *Chem. Phys. Lett.*, 2008, **463**, 124–129.
37 X. Lepró, Y. Vega-Cantú, F. J. Rodríguez-Macías, Y. Bando, D. Golberg and M. Terrones, Production and Characterization of Coaxial Nanotube Junctions and Networks of CN x/CNT, *Nano Lett.*, 2007, **7**, 2220–2226.
38 T. Wu, S. Zhu, Y. Xie, Q. Ma and C. Lu, NaNO3 assisted gelatin-derived multi-level porous carbon aerogel loaded Fe single-atom for high efficient oxygen reduction reaction, *Appl. Catal., B*, 2023, **331**, 122685.
39 A. Kandasamy, T. Ramasamy, A. Samrin, P. Narayanasamy, R. Mohan, O. Bazaka, I. Levchenko, K. Bazaka and M. Mohandas, Hierarchical Doped Gelatin-Derived Carbon Aerogels: Three Levels of Porosity for Advanced Supercapacitors, *Nanomaterials*, 2020, **10**, 1178.
40 X. Xue, W. Yuan, Z. Zheng, J. Zhang, C. Ao, J. Zhao, Q. Wang, W. Zhang and C. Lu, Iron-Loaded Carbon Aerogels Derived from Bamboo Cellulose Fibers as Efficient Adsorbents for Cr(VI) Removal, *Polymers*, 2021, **13**, 4338.
41 E. R. Edwards, E. F. Antunes, E. C. Botelho, M. R. Baldan and E. J. Corat, Evaluation of residual iron in carbon nanotubes purified by acid treatments, *Appl. Surf. Sci.*, 2011, **258**, 641–648.
42 M. A. Worsley, M. Stadermann, Y. M. Wang, J. H. Satcher Jr. and T. F. Baumann, High surface area carbon aerogels as porous substrates for direct growth of carbon nanotubes, *Chem. Commun.*, 2010, **46**, 9253.
43 L.-H. Lai, J.-S. Yang and S.-T. Shiue, Characteristics of carbon films prepared by thermal chemical vapor deposition using camphor, *Thin Solid Films*, 2014, **556**, 544–551.

44 J. Ekspong, E. Gracia-Espino and T. Wågberg, Hydrogen Evolution Reaction Activity of Heterogeneous Materials: A Theoretical Model, *J. Phys. Chem. C*, 2020, **124**, 20911–20921.
45 J. Ekspong, N. Boulanger and E. Gracia-Espino, Surface activation of graphene nanoribbons for oxygen reduction reaction by nitrogen doping and defect engineering: An ab initio study, *Carbon*, 2018, **137**, 349–357.
46 X. Xue, W. Yuan, Z. Zheng, J. Zhang, C. Ao, J. Zhao, Q. Wang, W. Zhang and C. Lu, Iron-Loaded Carbon Aerogels Derived from Bamboo Cellulose Fibers as Efficient Adsorbents for Cr(VI) Removal, *Polymers*, 2021, **13**, 4338.
47 H.-T. Fang, C.-G. Liu, C. Liu, F. Li, M. Liu and H.-M. Cheng, Purification of Single-Wall Carbon Nanotubes by Electrochemical Oxidation, *Chem. Mater.*, 2004, **16**, 5744–5750.
48 D. K. Sam, W. Wang, S. Gong, E. K. Sam, X. Lv, J. Wang and J. Liu, CO2 assisted synthesis of silk fibroin driven robust N-doped carbon aerogels coupled with nickel–cobalt particles as highly active electrocatalysts for HER, *Int. J. Hydrogen Energy*, 2021, **46**, 21525–21533.
49 B. Hui, H. Chen, C. Zhou, L. Cai, K. Zhang, F. Quan and D. Yang, Biochar aerogel-based electrocatalyst towards efficient oxygen evolution in acidic media, *Biochar*, 2022, **4**, 39.
50 J. E. Omoriyekomwan, C. He, L. Fan and A. Folli, Biomass-derived carbon nanostructures and their applications as electrocatalysts for hydrogen evolution and oxygen reduction/evolution, *Front. Environ. Eng.*, 2023, **2**, 1228992.